JACS
JOURNAL OF THE AMERICAN CHEMICAL SOCIETY
Article
pubs.acs.org/JACS

$Ca_{1-x}RE_xAg_{1-y}Sb$ (RE = La, Ce, Pr, Nd, Sm; $0 \le x \le 1$; $0 \le y \le 1$): Interesting Structural Transformation and Enhanced High-Temperature Thermoelectric Performance

Jian Wang, Xiao-Cun Liu, Sheng-Qing Xia,* and Xu-Tang Tao*

State Key Laboratory of Crystal Materials, Institute of Crystal Materials, Shandong University, Jinan, Shandong 250100, People's Republic of China

Supporting Information

ABSTRACT: For materials used in high-temperature thermoelectric power generation, the choices are still quite limited. Here we demonstrate the design and synthesis of a new class of complex Zintl compounds, $Ca_{1-x}RE_xAg_{1-y}Sb$ (RE = La, Ce, Pr, Nd, Sm) ($P6_3mc$, No. 186, LiGaGe-type), which exhibit a high figure of merit in the high-temperature region. Compared with the parent structure that is based on CaAgSb (*Pnma*, No. 62, TiNiSi-type), an interesting structural relationship is established which suggests that important size and electronic effects govern the formation of these multinary phases. According to theoretical calculations, such a structural transformation from the orthorhombic TiNiSi-type to the hexagonal LiGaGe-type also corresponds to an obvious modification in the electronic band structure, which explains the observed significant enhancement of the related thermoelectric properties. For an optimized p-type material, $Ca_{0.84}Ce_{0.16}Ag_{0.87}Sb$, a figure of merit of ~0.7 can be achieved at 1079 K, which is comparable to that of $Yb_{14}MnSb_{11}$ at the same temperature. In addition, due to the excellent thermal stability and high electrical conductivity, these materials are very promising candidates for high-temperature thermoelectric power generation.

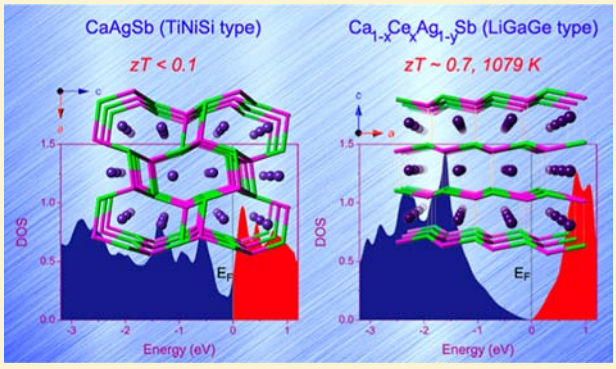

INTRODUCTION

Thermoelectric materials play a key role in current energy-saving efforts by converting waste heat into reusable electricity.[1−3] The application of such materials is limited mainly by their low energy conversion efficiency, which is evaluated through the dimensionless figure of merit $zT = \alpha^2\sigma T/\kappa$, where α is the Seebeck coefficient, T is the temperature, σ is the electrical conductivity, and κ is the thermal conductivity. Ideally, a good thermoelectric material should possess a large Seebeck coefficient, high electrical conductivity, and in the meantime low thermal conductivity. However, the real situation is that these variables are usually interrelated to each other via carrier concentration and band structure, which makes the maximization of zT a compromised result of these physical properties.[4−6] On the basis of this knowledge, various strategies have been introduced to design new thermoelectrics,[5−8] and many state-of-the-art high-zT materials, especially for chalcogenide-based compounds,[9−20] have been developed and successfully used in the midtemperature range (500−900 K) during the past decade.[21,22]

Despite the rapid progress mentioned above, in the case of high-temperature (>900 K) thermoelectric power generation, there is still a lack of suitable materials.[22,23] For currently used silicon−germanium alloys, the zT value is fairly low due to the relatively high lattice thermal conductivity of the diamond structure.[24] For *p*-SiGe used by NASA, the material only reaches a maximum figure of merit of just over 0.5 at 1100 K.[24] Very recently, with the discovery of a new high-temperature thermoelectric material $Yb_{14}MnSb_{11}$,[23,25] a breakthrough has been made which also focused interest in the search for new thermoelectrics based on Zintl compounds. For example, high zT values of around 1.0 were frequently observed for optimized bulk $Yb_{14}MnSb_{11}$ materials.[23,25] In addition, many other Zintl systems such as Ca_3AlSb_3,[26] Sr_3GaSb_3,[27] AT_2Sb_2 (A = Ca, Yb, Sr, Eu, Ba; T = Mn, Zn, Cd),[28−34] $Ca_5Al_2Sb_6$,[35] $Yb_{11}InSb_9$[36] have been carefully explored with much constructive and insightful work reported.

Here we demonstrate the design and synthesis of a series of new complex Zintl phases, $Ca_{1-x}RE_xAg_{1-y}Sb$ (RE = La, Ce, Pr, Nd, Sm), whose structure is derived from a simple ternary system CaAgSb.[37] The latter can be viewed as a Zintl compound with nominal oxidation states assigned as $[Ca^{2+}]$ $[Ag^{+}]$ $[Sb^{3-}]$. An introduction of trivalent cations to the calcium site will result in electron excess in the whole system, which is thus compensated by creating defects on the silver cation sites. Interestingly, such a delicate modification can turn the orthorhombic TiNiSi-type parent structure into a new hexagonal LiGaGe-type. Such structural changes also correspond to significant enhancement of the related thermoelectric

Received: April 15, 2013
Published: July 19, 2013

   dx.doi.org/10.1021/ja403653m | J. Am. Chem. Soc. 2013, 135, 11840−11848

properties and are well understood in light of theoretical calculations, which suggest important size and electronic effects. The optimized p-type material $Ca_{0.84}Ce_{0.16}Ag_{0.87}Sb$ has a figure of merit of about 0.7 at 1079 K, a value which is 6 times higher than the maximum zT value of CaAgSb and comparable as well with that of $Yb_{14}MnSb_{11}$ at the same temperature.[23,25] In additional to high figure of merit, these materials also exhibit excellent thermal stability, and unlike $Yb_{14}MnSb_{11}$, the crystals are quite stable in air which makes them very easy to work with. Another advantage lies in their metallic electrical conduction, which is especially important in configuring thermoelectric power generators with low internal resistance. The report of current work will not only provide a rich source of promising candidates for high temperature thermoelectric applications but also present new ideas on the design of high zT state-of-art materials in this field.

EXPERIMENTAL SECTION

Synthesis. All synthesis processes were conducted in an argon-filled glovebox or under vacuum. Starting materials were commercial grade and used as received: Ca (Alfa, shot, 99.5%, metals basis), Ag (Alfa, shot, 99.99%, metals basis), Sb (Alfa, shot, 99.999%, metals basis), Pb (Alfa, granules, 99.99%, metals basis), La (Alfa, rod, 99.9%, metals basis), Ce (Alfa, ingot, 99.8%), Pr (Alfa, ingot, 99.9%), Nd (Alfa, ingot, 99.9%), Sm (Alfa, ingot, 99.9%).

Pb-flux reactions were utilized to explore possible phases related to the $Ca_{1-x}RE_xAg_{1-y}Sb$ system. The first compound obtained was the La-containing antimonide $Ca_{0.89(1)}La_{0.11(1)}Ag_{0.92(2)}Sb$, in a loading ratio of Ca:La:Ag:Sb:Pb = 1:1:1:1:10 with synthesis procedure as follows: the reactants were loaded in an alumina crucible which was subsequently sealed in an evacuated, fused, silica jacket. The container was then moved into a programmable furnace. The reaction mixture was first heated to 900 °C at a rate of 200 °C/h and then homogenized at this temperature for 24 h; after the dwelling procedure, it was slowly cooled down to 600 °C at a rate of 5 °C/h; at this temperature, the excess molten Pb-flux was immediately decanted by centrifuge, and the product was a mixture of the title compound and the orthorhombic CaAgSb[37] phase. After the structure and composition were determined by single-crystal X-ray diffraction and EDS analysis, a stoichiometric ratio of Ca:La:Ag:Sb:Pb = 0.9:0.1:0.9:1:10 was then applied to repeat the reaction, and the title compound was reproduced in a state of high purity. For extending this system to contain other possible rare-earth metals, Ce, Pr, Nd and Sm were successfully incorporated to form new phases isotypic to the title compound. However, for the rest of the rare-earth elements, such as Tb, Dy, Ho, Er, Tm, and Lu, the main products are still the orthorhombic CaAgSb phase,[37] and no target compounds were found in those reactions.

Powder X-ray Diffraction. For phase identification, powder X-ray diffraction patterns were recorded at room temperature on a Bruker AXS X-ray powder diffractometer using Cu Kα radiation. The data were recorded in the 2θ mode with a step size of 0.02°, and the counting time was set to 10 s.

Single-Crystal X-ray Diffraction. Crystals with suitable size were selected and cut under the microscope. Since all title compounds are stable in air, the data collection was done without any inert gas protection at room temperature with a Bruker SMART APEX-II CCD area detector on a D8 goniometer using graphite-monochromated Mo Kα radiation (λ = 0.71073 Å). Data reduction and integration, together with global unit cell refinements were done by the INTEGRATE program of the APEX2 software.[38] Semi-empirical absorption corrections were applied using the SCALE program for area detector.[39] The structures were solved by direct methods and refined by the full matrix least-squares methods on F^2 using SHELX.[39] In the last refinement cycles, the atomic positions for the compounds were standardized using the program Structure TIDY.[40,41] All structures were refined to convergence with anisotropic displacement parameters. Other details on structure solving and refinement are provided in the Supporting Information. Further information in the form of CIF files has been deposited with Fachinformationszentrum Karlsruhe, 76344 Eggenstein-Leopoldshafen, Germany (Fax: (49) 7247-808-666; e-mail: crysdata@fiz-karlsruhe.de); depository CSD-number 426016 for $Ca_{0.89(1)}La_{0.11(1)}Ag_{0.92(2)}Sb$, 426017 for $Ca_{0.84(1)}Ce_{0.16(1)}Ag_{0.90(2)}Sb$, 426018 for $Ca_{0.87(1)}Pr_{0.14(1)}Ag_{0.86(1)}Sb$, 426019 for $Ca_{0.86(1)}Nd_{0.14(1)}Ag_{0.87(1)}Sb$, and 426020 for $Ca_{0.83(1)}Sm_{0.17(1)}Ag_{0.88(2)}Sb$, respectively.

Elemental Analysis. Energy dispersive X-ray spectroscopy (EDS) was taken on selected single crystals with a Hitachi FESEM-4800 field emission microscope equipped with a Horiba EX-450 EDS. For detection of the different compositions in $Ca_{1-x}Ce_xAg_{1-y}Sb$ materials, Rigaku/Fully Automated Sequential X-ray Fluorescence Spectrometer System (Primus II) was used.

Magnetic Susceptibility Measurements. Field-cooled DC magnetization measurements on a polycrystalline sample of $Ca_{0.84(1)}Ce_{0.16(1)}Ag_{0.90(2)}Sb$ (mass: 23.3 mg) were performed in a Quantum Design PPMS SQUID magnetometer. The applied magnetic field was 5000 Oe with the temperature ranging from 5 to 300 K. The raw data were corrected for the diamagnetic contribution of the holder and converted to molar susceptibility.

Thermal Analysis. Thermogravimetric (TG) and differential scanning calorimetry (DSC) analyses were taken on a Mettler-Toledo TGA/DSC/1600HT instrument. The measurements were done under the protection of high-purity argon gas flow from 300 to 1373 K, and the rate of temperature increase was 10 K/min.

SPS Experiments. The $Ca_{1-x}RE_xAg_{1-y}Sb$ polycrystalline samples (mass: ~2.5g) were carefully ground into a fine powder in the glovebox and then sintered at 1273 K through spark plasma sintering (SPS 1050: Sumitomo Coal Mining Co, Ltd.) for 5 min with a uniaxial pressure of 40 MPa to form pellets of about ⌀ 12.5 mm × 2.5 mm. The density of all the pellets was >95% of the theoretical value. All pellets were polished in the glovebox to avoid possible surface contamination. The sample purity after SPS was checked by powder X-ray diffraction, and the patterns were in good agreement with the positions of the theoretical Bragg reflections.

Thermal Conductivity. Thermal conductivity was measured on disk samples (⌀ 12.5 mm) of $Ca_{1-x}RE_xAg_{1-y}Sb$ in an argon atmosphere by using a NETZSCH LFA457 instrument. The measurements were performed in a temperature range from 323 to 1079 K and a standard sample of pyroceram 9606 (⌀ 12.7 mm × 1.98 mm) was used as the reference for measuring the heat capacity. The thermal conductivity was calculated from: $\kappa = D \times \rho \times C_p$ (D: thermal diffusivity; ρ: density; C_p: heat capacity).

Seebeck Coefficient and Resistivity. After the thermal conductivity measurements were completed, the sample pellet was cut into bars of suitable size to perform the Seebeck coefficient and electrical conductivity measurements. These two physical properties were measured simultaneously over the temperature range of 300 to 1079 K with a Linseis LSR-3/1100 instrument system in helium atmosphere.

Computational Details. To better understand the unusual structure and properties related to these new phases, density functional calculations were performed on a hypothetical hexagonal CaAgSb structure, constructed from $Ca_{0.89(1)}La_{0.11(1)}Ag_{0.92(2)}Sb$, by assuming a rigid band structure model. The original orthorhombic CaAgSb structure was analyzed as well for comparison. The full potential linearized augmented plane wave method (FP-LAPW)[42,43] was applied with the aid of Wien2k code.[44] In this method, the unit cell is divided into nonoverlapping muffin-tin (MT) spheres and an interstitial region. The wave functions in the interstitial regions are expanded in plane waves up to $R_{MT} \times K_{max} = 7$, where R_{MT} is the smallest radius of all MT spheres, and K_{max} is the plane wave cutoff. The valence wave functions inside the MT spheres are expanded up to $l_{max} = 10$ while the charge density was Fourier expanded up to $G_{max} = 12$ (au)$^{-1}$. The MT radii were chosen to be 2.3 b for both Ca and Ag, and 2.5 b for Sb. The exchange correlation potential was calculated using the Perdew–Burke–Ernzerhof generalized gradient approximation (PBE-GGA).[45] Self-consistency was achieved using 1000 k-points in the irreducible Brillouin zone (IBZ). The BZ integration was performed using the

Table 1. Selected Crystal Data and Structure Refinement Parameters for $Ca_{1-x}RE_xAg_{1-y}Sb$ (RE = La, Ce, Pr, Nd, Sm)

formula	$Ca_{0.89(1)}La_{0.11(1)}Ag_{0.92(2)}Sb$	$Ca_{0.84(1)}Ce_{0.16(1)}Ag_{0.90(2)}Sb$	$Ca_{0.87(1)}Pr_{0.14(1)}Ag_{0.86(1)}Sb$	$Ca_{0.86(1)}Nd_{0.14(1)}Ag_{0.87(1)}Sb$	$Ca_{0.83(1)}Sm_{0.17(1)}Ag_{0.88(2)}Sb$
fw/g·mol^{-1}	271.45	274.92	267.67	269.72	275.50
T/K			293(2)		
radiation, wavelength			Mo Kα, 0.71073 Å		
space group			$P6_3mc$ (No. 186)		
Z			2		
unit cell dimensions					
a / Å	4.7029(8)	4.7023(6)	4.7057(5)	4.6931(12)	4.7008(9)
c / Å	7.7921(18)	7.7951(11)	7.7880(17)	7.753(2)	7.759(3)
V/Å^3	149.25(5)	149.27(3)	149.35(4)	147.89(7)	148.49(7)
ρ_{calc}/g·cm^{-3}	6.040	6.117	5.952	6.057	6.162
$\mu_{Mo\ K\alpha}$/cm^{-1}	177.50	184.41	179.61	184.25	192.98
final R indices[a] [$I > 2\sigma_{(I)}$]	R_1 = 0.0256	R_1 = 0.0194	R_1 = 0.0227	R_1 = 0.0234	R_1 = 0.0267
	wR_2 = 0.0607	wR_2 = 0.0492	wR_2 = 0.0545	wR_2 = 0.0441	wR_2 = 0.0621
final R indices[a] [all data]	R_1 = 0.0287	R_1 = 0.0207	R_1 = 0.0253	R_1 = 0.0297	R_1 = 0.0325
	wR_2 = 0.0624	wR_2 = 0.0499	wR_2 = 0.0553	wR_2 = 0.0464	wR_2 = 0.0598

[a] $R_1 = \sum||F_o| - |F_c||/\sum|F_o|$; $wR_2 = [\sum[w(F_o^2 - F_c^2)^2]/\sum[w(F_o^2)^2]]^{1/2}$, and $w = 1/[\sigma^2F_o^2 + (A\cdot P)^2 + B\cdot P]$, $P = (F_o^2 + 2F_c^2)/3$; A and B are weight coefficients.

tetrahedron method, and the self-consistent calculations are considered to have converged if the total energy and the charge of the system are stable within 10^{-4} Ry and 10^{-4} e$^-$, respectively.

RESULTS AND DISCUSSION

Structure Description. All $Ca_{1-x}RE_xAg_{1-y}Sb$ (RE = La, Ce, Pr, Nd, Sm) compounds crystallize in the same structure type, and details of the data collection and structure refinement are listed in Table 1. For clarity, only $Ca_{0.89(1)}La_{0.11(1)}Ag_{0.92(2)}Sb$ is discussed for structure description here, and its positional and equivalent isotropic displacement parameters and important bond distances are tabulated in Tables 2 and 3, respectively. Data on the other crystals are provided in Tables S1 and S2 (Supporting Information).

Table 2. Refined Atomic Coordinates and Isotropic Displacement Parameters for $Ca_{0.89\ (1)}La_{0.11(1)}Ag_{0.92(2)}Sb$

atoms	Wyckoff	x	y	z	U_{eq}[a] (Å^2)	occupancy
Ca	2a	0	0	−0.0027(4)	0.0211(11)	0.89(1)
La	2a	0	0	−0.0027(4)	0.0211(11)	0.11(1)
Ag	2b	1/3	2/3	0.7030(3)	0.0351(11)	0.92(2)
Sb	2b	1/3	2/3	0.27260(5)	0.0153(4)	1

[a] U_{eq} is defined as one-third of the trace of the orthogonalized U^{ij} tensor.

Table 3. Important Interatomic Distances (Å) in $Ca_{0.89(1)}La_{0.11(1)}Ag_{0.92(2)}Sb$

atom pairs	distances (Å)	atom pairs	distances (Å)
Ca/La − Sb × 3	3.231(2)	Ag − Sb × 3	2.7688(7)
Sb × 3	3.460(2)	Sb	3.354(3)
Ag × 3	3.153(2)		
Ag × 3	3.554(3)		

$Ca_{0.89(1)}La_{0.11(1)}Ag_{0.92(2)}Sb$ adopts the hexagonal system with space group $P6_3mc$, which is isotypic to the LiGaGe structure type.[46,47] The structure can be concisely described as stacked with a series of puckered [AgSb] layers, which are sandwiched by the Ca^{2+}/La^{3+} cations, as shown in Figure 1. These layers are further connected through Ag−Sb bonds along the direction of c-axis, and such interactions, with a long interatomic distance of

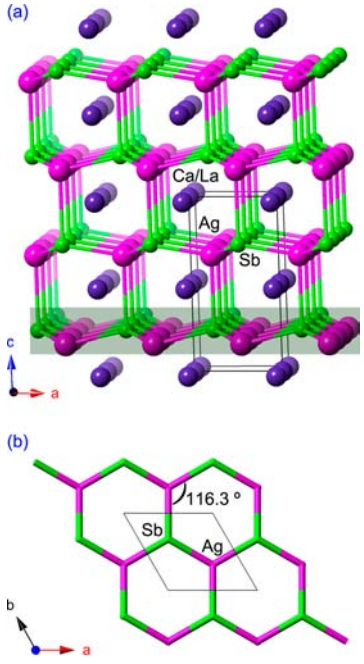

Figure 1. (a) Ball-and-stick representation of the crystal structure of $Ca_{0.89(1)}La_{0.11(1)}Ag_{0.92(2)}Sb$ viewed along the b-axis with [AgSb] layer emphasized in shadow area. Bonded Ag and Sb atoms are shown as magenta and green spheres, respectively, and mixed Ca/La sites are drawn in dark purple. (b) Schematic view of [AgSb] net with structure plotted in stick mode for better illustration.

3.354(3) Å, should be very weak if compared with the intralayer interactions for which a much shorter interatomic distance 2.7688(7) Å is observed. Another interesting aspect of this structure lies in the almost coplanar [AgSb] layer, which highly resembles honeycomb slabs of graphite with an in-plane Sb−Ag−Sb angle of 116.3°. The defects on the Ag sites can be understood by using the Zintl concepts: for undoped CaAgSb, it can be rewritten as a charge-balanced compound $[Ca^{2+}][Ag^+][Sb^{3-}]$, which means doping trivalent rare-earth metals on the cation sites will result in an electron excess, and this can be compensated by introducing additional silver defects. Actually, a simple electron counting on the above La-doped compound also results in an electron-precise system

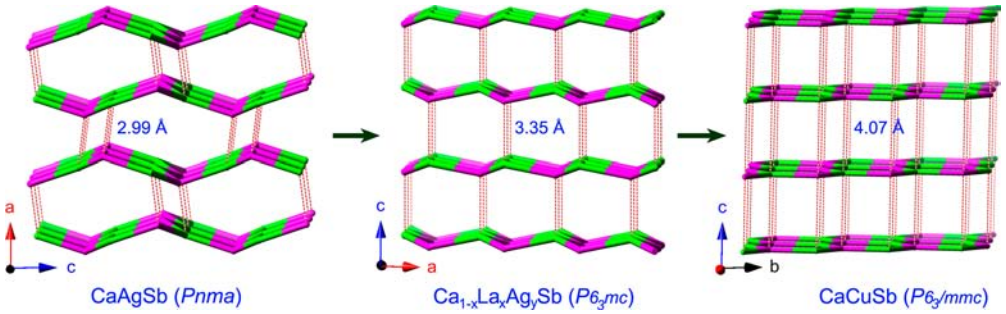

Figure 2. Side-by-side comparison of polyanion structures based on several closely related antimonide compounds. Graph indicates interesting structural evolution from orthorhombic TiNiSi-type CaAgSb to hexagonal graphitic CaCuSb with the intermediate structure of LiGaGe-type $Ca_{1-x}La_xAg_ySb$. Different interlayer Ag−Sb distances are also compared.

$[Ca^{2+}]_{0.9}[La^{3+}]_{0.1}Ag_{0.9}Sb$, whose composition is further evidenced by the theoretical calculations below and the EDS measurements (Supporting Information).

A side-by-side comparison of the polyanion structures of $Ca_{1-x}La_xAg_{1-y}Sb$ and other closely related phases CaMSb (M = Ag or Cu)[37,47,48] are also provided in Figure 2. For better illustration, all cations are removed, and the polyanion framework is drawn in stick mode with the interlayer M−Sb pairs connected by dashed lines. The picture demonstrates an interesting structural evolution from the orthorhombic puckered framework to a hexagonal graphitic layer. For CaAgSb, a short interlayer Ag−Sb distance 2.99 Å is observed, and although it is a little longer compared to the intralayer distance (2.836 Å), strong covalent bonding can still be expected between these [AgSb] slabs. While for CaCuSb, the graphite-like [CuSb] layers are well separated where the corresponding Cu and Sb atoms are found a distance of 4.07 Å away from each other. Thus, the structure of $Ca_{1-x}La_xAg_{1-y}Sb$, which bears less puckered and not significantly separated [AgSb] layers, actually represents an intermediate state between the structures of CaAgSb and CaCuSb.

The above discussion also suggests interesting size and electronic effects on the structural formation of these new phases. As indicated by the synthesis experiments, only large rare-earth cations, specifically from La^{3+} to Sm^{3+}, could be doped into the Ca^{2+} sites to form the $Ca_{1-x}RE_xAg_{1-y}Sb$ compounds. However, for those cations with sizes smaller than that of Ca^{2+} such as Tb^{3+}, Dy^{3+}, Ho^{3+}, Er^{3+}, Tm^{3+}, and Lu^{3+},[49−51] the orthorhombic CaAgSb remained the major product, and no new hexagonal phases were identified. These results can be easily understood from the fact that the puckered [AgSb] layers in $Ca_{1-x}RE_xAg_{1-y}Sb$ have larger separation distances than those of undoped CaAgSb, in which case large cations should favor the structural transformation after doping. Such separation distances are obviously dominated by the size of the doping cations, which can be evaluated using the *c*-axis cell parameter. Taking $Ca_{0.89(1)}La_{0.11(1)}Ag_{0.92(2)}Sb$ and $Ca_{0.83(1)}Sm_{0.17(1)}Ag_{0.88(2)}Sb$ as examples, the former has a much larger *c*-parameter value of 7.7921(18) Å compared to 7.759(3) Å for the latter. Certainly, the doping concentration should also play an important role; $Ca_{0.84(1)}Ce_{0.16(1)}Ag_{0.90(2)}Sb$, which has a smaller doping cation than $Ca_{0.89(1)}La_{0.11(1)}Ag_{0.92(2)}Sb$, exhibits an actually larger *c*-parameter due to the obviously higher doping concentration. The electronic effect related to the orthorhombic TiNiSi-type has been broadly discussed in the literature. This system represents a very electronically flexible family, accommodating from 15 to 18 electrons per formula.[47,52,53] A structural transformation may take place with more electrons introduced, i.e., LaNiSn[54] and CeIrAl[55] where both change from the orthorhombic TiNiSi-type to a hexagonal graphitic layer structure with the addition of hydrogen/deuterium into their lattices. In the current case of $Ca_{1-x}RE_xAg_{1-y}Sb$, the electronic effect is obviously different since the whole system retains 18 electrons. The extensive lattice defects and bond distortions, which are closely related to the structural formation, apparently cannot be explained by simple electron counting. Thus, more in-depth theoretical studies are necessary, and the results are provided below.

Theoretical Calculations. To better understand the electronic effects related to these interesting new phases, electronic band structure calculations were performed on two different structures, the orthorhombic TiNiSi-type CaAgSb and the hexagonal LiGaGe-type $Ca_{1-x}La_xAg_ySb$. A side-by-side comparison illustrated in Figure 3 shows that the related

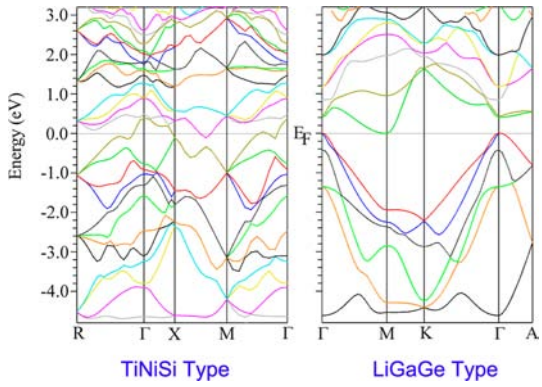

Figure 3. Electronic band structures calculated for orthorhombic TiNiSi-type CaAgSb (left) and hypothetical hexagonal LiGaGe-type $Ca_{1-x}La_xAg_ySb$ (right).

electronic band structures are significantly different despite identical valence electron concentration: the TiNiSi-type CaAgSb is metallic conducting with the conduction bands and the valence bands obviously overlapped at the Fermi level; while for the LiGaGe-type $Ca_{1-x}La_xAg_ySb$, a small band gap appears instead, and the compound turns out to be an indirect semiconductor. In addition, the bands in the vicinity of Fermi level also have very different dispersions. For the TiNiSi-type CaAgSb, the bands below the Fermi level are fairy dispersive, and it becomes much narrower in the LiGaGe-type $Ca_{1-x}La_xAg_ySb$. Combined with the calculated total and projected density of states presented in Figure 4, the bands

dx.doi.org/10.1021/ja403653m | J. Am. Chem. Soc. 2013, 135, 11840−11848

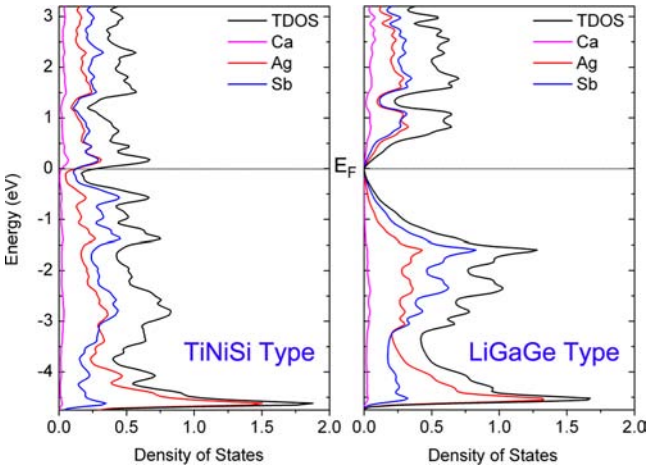

Figure 4. Total and projected density of states (DOS) for orthorhombic TiNiSi-type CaAgSb (left) and hypothetical hexagonal LiGaGe-type $Ca_{1-x}La_xAg_ySb$ (right).

right below the Fermi level are predominantly contributed by the Ag and Sb atoms, more specifically the bonding states related to the [AgSb] networks. With this analysis, it is expected that the intralayer Ag−Sb bonds in the LiGaGe-type $Ca_{1-x}La_xAg_ySb$ are much stronger than those of the TiNiSi-type CaAgSb. These results are also well supported by the crystallographic data, i.e., for CaAgSb the corresponding Ag−Sb bond length is about 2.836 Å, whereas it shortens to 2.7688(7) Å in $Ca_{0.89(1)}La_{0.11(1)}Ag_{0.92(2)}Sb$.

The above results suggest a very interesting electronic effect in the $Ca_{1-x}RE_xAg_{1-y}Sb$ series. By doping with the RE^{3+} cations, the original overlapped conduction bands and valence bands in undoped CaAgSb are now well separated with more bonding states contributing to the [AgSb] layers. Since the total electron number remains unchanged, such an enhancement of intralayer Ag−Sb interactions occurs at the cost of reducing the bonding electrons from the interlayer Ag−Sb bonds, which in turn substantially weakens the corresponding interactions. The electronic effect also leads to a large slope of the density of states below the Fermi level in the $Ca_{1-x}RE_xAg_{1-y}Sb$ structure. For the TiNiSi-type CaAgSb the states below the Fermi level are very dispersive; however, they form a broad sharp peak with much higher intensity for the LiGaGe-type $Ca_{1-x}La_xAg_ySb$. Such a characteristic shall favor high figure of merit according to recent theoretical studies.[12,21,56]

On the basis of the above discussion, the $Ca_{1-x}RE_xAg_{1-y}Sb$ series appears to be a perfect candidate for designing state-of-the-art thermoelectric materials. Their crystal and electronic structures are delicately governed by size and electronic effects that originate with the doping cations. Through varying the type and concentration of the doping cations, both interlayer and intralayer Ag−Sb interactions can be easily adjusted, which significantly affects the electronic band structure and the related thermoelectric properties. Moreover, the electron tuning of $Ca_{1-x}RE_xAg_{1-y}Sb$ is very flexible—one can choose either the calcium site or the silver site for optimizing the carrier concentration. With such a highly disordered structure, low lattice thermal conductivity can be expected, and thus the advantages of these new phases as new thermoelectric materials are obvious.

Thermal Stability. It is not surprising to observe excellent thermal stability in the $Ca_{1-x}RE_xAg_{1-y}Sb$ series. Many related complex antimonide Zintl phases, such as $Yb_{14}MnSb_{11}$,[23] $A_{10}LaCdSb_9$ (A = Ca, Yb),[57] $Yb_{11}TrSb_9$ (Tr = Ga, In),[36] have already been reported to be thermally stable up to very high temperature. The typical TG-DSC behavior, represented by $Ca_{0.84(1)}Ce_{0.16(1)}Ag_{0.90(2)}Sb$, is shown in Figure 5 and compared

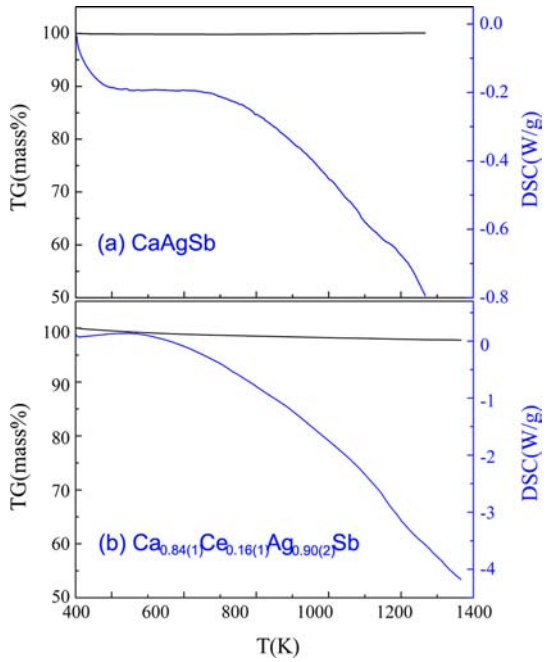

Figure 5. TG-DSC measurements on undoped CaAgSb and Ce-doped $Ca_{0.84(1)}Ce_{0.16(1)}Ag_{0.90(2)}Sb$, conducted in inert argon atmosphere over the temperature range of 300−1373 K.

side-by-side with that of the undoped CaAgSb compound. The TG curves indicate negligible weight loss in the measured temperature range (300−1373 K), and no melting or phase transition processes can be identified from the corresponding DSC data.

Preparation of $Ca_{1-x}Ce_xAg_{1-y}Sb$ materials. The $Ca_{1-x}Ce_xAg_{1-y}Sb$ series were chosen for systematic thermoelectric property studies since these materials can be easily purified, probably because Ce has the lowest melting point compared to the other rare-earth metals. In this work, materials with different Ag concentration, $Ca_{0.84}Ce_{0.16}Ag_{1-y}Sb$ ($0.10 \leq y \leq 0.15$), were synthesized, and their thermoelectric properties were probed. For higher or lower level of silver composition, the products tend to have a considerable number of impurities, as suggested by the powder X-ray diffraction patterns (Figure 6). The undoped TiNiSi-type CaAgSb was also synthesized for property comparison. In order to strictly control the compositions of various materials, the weighting errors of each element were limited to be less than 0.1%, and X-ray fluorescence (XRF) technique was applied to characterize the different Ag levels.

Materials for thermoelectric property studies were all prepared from the Nb-tube reactions. In order to obtain samples with high purity and eliminate the orthorhombic CaAgSb impurity, a two-step synthesis method was utilized and proved to be very successful in synthesizing the Ce-doped compounds. The procedure can be described as follows: the metal elements were first loaded in a Nb tube with the stoichiometric ratio; then the Nb tube was enclosed by arc-welding in the glovebox and subsequently sealed in an

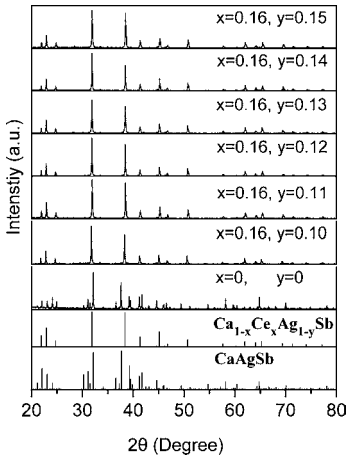

Figure 6. Powder XRD patterns for various $Ca_{1-x}Ce_xAg_{1-y}Sb$ phases obtained from on-stoichiometric reactions in Nb tubes. Calculated patterns for undoped TiNiSi-type CaAgSb and Ce-doped LiGaGe-type $Ca_{1-x}Ce_xAg_{1-y}Sb$ are shown for reference as well.

evacuated fused silica jacket; the reaction mixture was heated to 1100 °C at a rate of 200 °C/h and then left to dwell for 96 h, followed by a slow cooling process to 800 °C at a rate of 3 °C/h, and finally annealed at this temperature for 2 days; the furnace was turned off, and the vessel was opened in the glovebox; the products were ground into fine powder and resealed into a new Nb tube to repeat the above synthesis steps. With such a procedure, the resulting product was a pure phase of the target compound, which was confirmed by powder X-ray diffraction pattern and the magnetic susceptibility measurements (Supporting Information). In order to better study the thermoelectric properties, the possible phase width related to the Ag defects was probed, and the results indicated a fairly narrow homogeneity range for $Ca_{0.84}Ce_{0.16}Ag_{1-y}Sb$ ($0.10 \leq y \leq 0.15$). The compositions of these materials were further characterized by using XRF, and a trend of the reducing Ag concentration was clear (Supporting Information).

Thermoelectric Properties. Temperature-dependent resistivity data are provided in Figure 7. It is not surprising to observe similar conduction behavior for all the related phases; with increasing temperature, the resistivity first increases and, after reaching a peak, starts to decrease slowly. It should be noted that the electrical properties of LiGaGe-type $Ca_{1-x}Ce_xAg_{1-y}Sb$ seem to be very sensitive to Ag defects, i.e., a few more silver defects than in $Ca_{0.84}Ce_{0.16}Ag_{0.90}Sb$ will

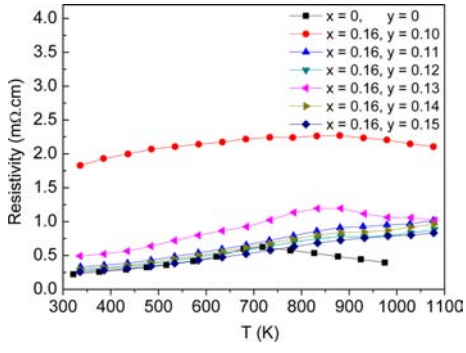

Figure 7. Resistivity measurements performed on various $Ca_{1-x}Ce_xAg_{1-y}Sb$ phases over temperature range of 323–1079 K under helium atmosphere.

significantly reduce the corresponding resistivity. However, such resistivity variations are not linearly dependent on the Ag-defect levels, which is probably due to the complicated crystal and electronic structures of these phases. Compared with $Yb_{14}MnSb_{11}$,[23] a highly efficient thermoelectric material with a resistivity of 2–5.4 mΩ.cm from 300 to 1200 K, the $Ca_{1-x}Ce_xAg_{1-y}Sb$ series has better electrical conduction. The resistivity of $Ca_{0.84}Ce_{0.16}Ag_{0.90}Sb$ is only 1.83 mΩ·cm at 335 K, and especially for materials with a higher Ag-defect level, the value is generally smaller than 1.0 mΩ·cm. The TiNiSi-type CaAgSb has an even smaller resistivity (~0.25 mΩ·cm at 335 K), which can be understood from its metallic conducting electronic band structure.

All $Ca_{1-x}Ce_xAg_{1-y}Sb$ phases are p-type materials, as suggested by their positive Seebeck coefficient plotted in Figure 8. The TiNiSi-type CaAgSb possesses a very low

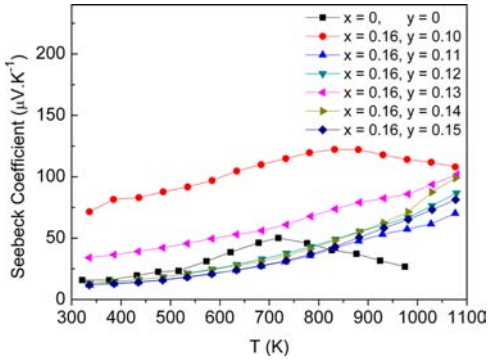

Figure 8. Seebeck coefficient data obtained for various $Ca_{1-x}Ce_xAg_{1-y}Sb$ phases over temperature range of 323–1079 K under helium atmosphere.

Seebeck coefficient, and only reaches a maximum value of 50 $\mu V \cdot K^{-1}$ at 718 K. When incorporated with Ce^{3+}, the materials show substantially enhanced Seebeck coefficient. For the specific composition $Ca_{0.84}Ce_{0.16}Ag_{0.90}Sb$, a value of 120 $\mu V \cdot K^{-1}$ has been achieved at 832 K. The higher Seebeck coefficient that is observed in $Ca_{1-x}Ce_xAg_{1-y}Sb$ is also supported by its electronic band structure, which indicates a good separation between the conduction bands and valence bands with a small band gap appearing at the Fermi level. Using the equation $E_g \approx 2e\alpha_{max}T_{max}$[58] as an estimate, a thermal activation band gap of 0.2 eV is obtained for $Ca_{0.84}Ce_{0.16}Ag_{0.90}Sb$. With the Ag-defect level increased, the corresponding Seebeck coefficient of $Ca_{1-x}Ce_xAg_{1-y}Sb$ changes behavior and the peak shifts to a higher temperature region that is not covered in the current measurement range.

The measured thermal conductivity for LiGaGe-type $Ca_{1-x}Ce_xAg_{1-y}Sb$ is very low, consistent with the highly disordered crystal structure. As presented in Figure 9, the thermal conductivity of $Ca_{0.84}Ce_{0.16}Ag_{0.90}Sb$ is only 0.603 $W \cdot m^{-1} \cdot K^{-1}$ at 335 K and reaches 1.40 $W \cdot m^{-1} \cdot K^{-1}$ at 1076 K. Similar to the resistivity and Seebeck coefficient data, the thermal conductivity of the $Ca_{1-x}Ce_xAg_{1-y}Sb$ series is also obviously affected by the silver defect level. Taking $Ca_{0.84}Ce_{0.16}Ag_{0.85}Sb$ as an example, the corresponding values range from 4.3 to 2.5 $W \cdot m^{-1} \cdot K^{-1}$ from 335 to 1076 K. More interestingly, there exist two different types of thermal conduction behavior, represented by cases with compositions of $y = 0.10$ and $0.11 \leq y \leq 0.15$. In the former, the thermal conductivity increases slowly with increasing temperature.

dx.doi.org/10.1021/ja403653m | J. Am. Chem. Soc. 2013, 135, 11840–11848

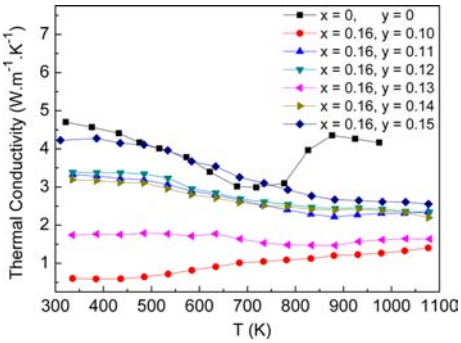

Figure 9. Measured thermal conductivity for various $Ca_{1-x}Ce_xAg_{1-y}Sb$ phases over temperature range of 323−1079 K under argon atmosphere.

However, for the rest compositions, the data possess decreasing thermal conductivity with increasing temperature. Although the trend of the thermal conductivity varied with different Ag concentration is not clear, the results collaborate well with the corresponding electrical properties: materials with high Seebeck coefficient and electrical resistivity will always lead to low thermal conductivity, and thus such behavior should be closely related to the thermal activation of the electrons. The lack of trend in physical properties with the varied compositions is very difficult to explain, however, the complicated electronic band structure of this system, especially when doped with Ce3+ ions, should play an important role. The lack of trend in physical properties has also been observed in some complex thermoelectric systems, such as $BiCu_{1-x}SeO$.[59] For TiNiSi-type CaAgSb, the thermal conductivity indicates a clear transition from 600 to 1000 K, which has not been reported before. According the DSC data, this process is not related to the structural change and is certainly worth further study. The thermal conductivity of the $Ca_{1-x}Ce_xAg_{1-y}Sb$ series is a little higher than some of the typical Zintl compound-based thermoelectric materials, such as $Yb_{14}MnSb_{11}$ (0.7 $W{\cdot}m^{-1}{\cdot}K^{-1}$ at 1100 K),[23] Sr_3GaSb_3 (0.6 $W{\cdot}m^{-1}{\cdot}K^{-1}$ at 1000 K),[27] $Ca_5Al_2Sb_6$ (0.8 $W{\cdot}m^{-1}{\cdot}K^{-1}$ at 850 K),[35] Zn_4Sb_3 (0.6 $W{\cdot}m^{-1}{\cdot}K^{-1}$ at 650 K).[60,61]

The figure of merit calculated for various $Ca_{1-x}Ce_xAg_{1-y}Sb$ materials is plotted in Figure 10. As suggested by the theoretical calculations, the hexagonal LiGaGe-type $Ca_{1-x}Ce_xAg_{1-y}Sb$ exhibits a much enhanced thermoelectric performance than

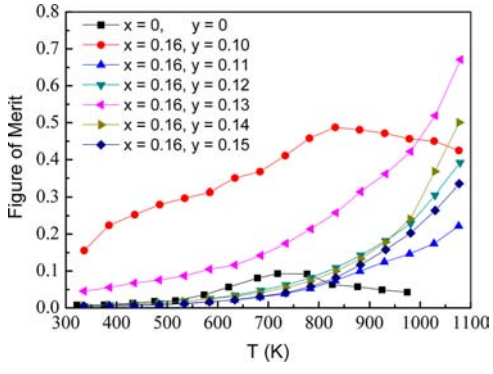

Figure 10. Figure of merit estimated for various $Ca_{1-x}Ce_xAg_{1-y}Sb$ materials. For optimized composition $Ca_{0.84}Ce_{0.16}Ag_{0.13}Sb$, the zT keeps increasing rapidly with increasing temperature and reaches a value of about 0.7 at 1079 K.

the orthorhombic TiNiSi-type CaAgSb. For a low Ag-defect level, a maximum zT of only 0.5 is observed at 832 K; however, for the optimized composition of $Ca_{0.84}Ce_{0.16}Ag_{0.87}Sb$, the zT increases rapidly with increasing temperature and reaches a value of about 0.7 at 1079 K, which is comparable with that of $Yb_{14}MnSb_{11}$ at the same temperature.[23,25] It can be expected that at higher temperatures these materials would exhibit even higher figure of merit. Unfortunately, such measurements are limited by currently used instruments, and the data cannot be provided. As a new class of thermoelectric materials, $Ca_{1-x}Ce_xAg_{1-y}Sb$ is a very promising candidate for high-temperature thermoelectric power generation due to the following advantages. First, these materials have excellent thermal stability and are very easy to handle since they are not sensitive to air. (Please note that the air stability only applies to near-room temperature conditions, whereas the advantageous thermoelectric properties show mainly at high temperatures for which air protection is still mandatory.) Second, unlike Si−Ge alloys, their mechanical properties are similar to those of metals, which makes them very flexible for manufacturing various shapes of devices; Third, their resistivity, i.e., 1.0 mΩ·cm at 1079 K for $Ca_{0.84}Ce_{0.16}Ag_{0.87}Sb$, is much lower compared to the values of 5.5 mΩ·cm and 5.0 mΩ·cm for SiGe and $Yb_{14}MnSb_{11}$ at 1100 K, respectively. This advantage is very competitive for configuring thermoelectric power generators.

In addition, the thermoelectric properties of this series of materials can be further improved by applying the following strategy: (1) Improving the power factor through chemical doping. The power factor of these materials still has great potential to increase due to their relatively low Seebeck coefficient. This strategy has been demonstrated in various antimonide-based thermoelectric materials such as $Yb_{14}Mn_{1-x}Al_xSb_{11}$,[25e] $Ca_{5-x}Na_xAl_2Sb_6$,[35] and Sr_3GaSb_3,[27] and can lead to significant property improvement. (2) Band structure engineering. Band structure engineering has been proven to be very successful in tuning the thermoelectric properties of PbTe-based alloys as well as other chalcopyrite-related materials.[12,62] The special size and electronic effects existing with the $Ca_{1-x}Re_xAg_{1-y}Sb$ structure will also provide many opportunities for designing materials with good thermoelectric properties. (3) Reducing the thermal conductivity. The thermal conductivity of this series of compounds is relatively high compared to that of other complex Zintl phases. The substitution of Ca by heavier cations such as Yb may provide a solution, which has been proven very efficiently in $Ca_{1-x}Yb_xZn_2Sb_2$[28] and $Yb_{14-x}Ca_xMnSb_{11}$.[63] Besides alloy scattering, nanostructuring may also be an efficient way of obtaining a lower thermal conductivity.

■ CONCLUSIONS

In conclusion, we demonstrate the design and synthesis of a new class of Zintl phase-based thermoelectric materials $Ca_{1-x}RE_xAg_{1-y}Sb$ (RE = La, Ce, Pr, Nd, Sm). A structural transformation from the orthorhombic TiNiSi-type to the hexagonal LiGaGe-type has been observed, which originates from interesting size and electronic effects. These materials exhibit excellent high-temperature thermoelectric properties, which are understood by incorporation of the theoretical calculations. The results suggest well-separated conduction bands and valence bands as well as a large density of states slope below the Fermi level. With obvious advantages, such as excellent stability, good electrical conduction, and high figure of

merit, these materials may find very promising applications in high-temperature thermoelectric power generation.

■ ASSOCIATED CONTENT

Supporting Information

The X-ray crystallographic files in CIF format for all title compounds; the refined atomic coordinates and important interatomic distances for $Ca_{0.84(1)}Ce_{0.16(1)}Ag_{0.90(2)}Sb$, $Ca_{0.87(1)}Pr_{0.14(1)}Ag_{0.86(1)}Sb$, $Ca_{0.86(1)}Nd_{0.14(1)}Ag_{0.87(1)}Sb$, and $Ca_{0.83(1)}Sm_{0.17(1)}Ag_{0.88(2)}Sb$, respectively; description of the structure solution and refinement on $Ca_{0.89(1)}La_{0.11(1)}Ag_{0.92(2)}Sb$; elemental analysis on single crystal of $Ca_{0.89(1)}La_{0.11(1)}Ag_{0.92(2)}Sb$; composition characterization of $Ca_{0.84}Ce_{0.16}Ag_{1-y}Sb$ by XRF; magnetic susceptibility data for $Ca_{0.84(1)}Ce_{0.16(1)}Ag_{0.90(2)}Sb$. This information is available free of charge via the Internet at http://pubs.acs.org.

■ AUTHOR INFORMATION

Corresponding Author

shqxia@sdu.edu.cn (S.Q.X.); txt@sdu.edu.cn (X.T.T.).

Notes

The authors declare no competing financial interest.

■ ACKNOWLEDGMENTS

This work is sponsored by the National Natural Science Foundation of China (Grant Nos. 20901047, 51271098, 51021062, 51272129), the 973 Program of the People's Republic of China (Grant No. 2010CB630702), the Shandong Provincial Natural Science Foundation (Grant No. ZR2010BM003), the Independent Innovation Foundation of Shandong University (IIFSDU), and the Program of Introducing Talents of Disciplines to Universities in China (111 Program No. b06017).

■ REFERENCES

(1) Tritt, T. M. *Science* **1996**, *272*, 1276.
(2) Bell, L. *Science* **2008**, *321*, 1457.
(3) DiSalvo, F. J. *Science* **1999**, *295*, 703.
(4) Nolas, G. S.; Sharp, J.; Goldsmid, H. J. *Thermoelectrics, Basic Principles and New Materials Developments*; Springer: New York, 2001.
(5) Rowe, D. M. *Thermoelectrics Handbook: Macro to Nano*; CRC/Taylor & Francis: Boca Raton, FL, 2006.
(6) Rowe, D. M. *CRC Handbook of Thermoelectrics*; CRC: Boca Raton, 1995.
(7) Shevelkov, A. V. *Russ. Chem. Rev.* **2008**, *77*, 1.
(8) Toberer, E. S.; May, A. F.; Snyder, G. J. *Chem. Mater.* **2010**, *22*, 625.
(9) Plirdpring, T.; Kurosaki, K.; Kosuga, A.; Day, T.; Firdosy, S.; Ravi, V.; Snyder, G. J.; Harnwunggmoung, A.; Sugahara, T.; Ohishi, Y.; Muta, H.; Yamanaka, S. *Adv. Mater.* **2012**, *24*, 3622.
(10) Poudel, B.; Hao, Q.; Ma, Y.; Lan, Y.; Minnich, A.; Yu, B.; Yan, X.; Wang, D.; Muto, A.; Vashaee, D.; Chen, X.; Liu, J.; Dresselhaus, M. S.; Chen, G.; Ren, Z. F. *Science* **2008**, *320*, 634.
(11) Hsu, K. F.; Loo, S.; Guo, F.; Chen, W.; Dyck, J. S.; Uher, C.; Hogan, T.; Polychroniadis, E. K.; Kanatzidis, M. G. *Science* **2004**, *303*, 818.
(12) Heremans, J. P.; Jovovic, V.; Toberer, E. S.; Saramat, A.; Kurosaki, K.; Charoenphakdee, A.; Yamanaka, S.; Snyder, G. J. *Science* **2008**, *321*, 554.
(13) Pei, Y. Z.; Shi, X. Y.; LaLonde, A.; Wang, H.; Chen, L. D.; Snyder, G. J. *Nature* **2011**, *473*, 66.
(14) Pei, Y. Z.; Lensch-Falk, J.; Toberer, E. S.; Medlin, D. L.; Snyder, G. J. *Adv. Funct. Mater.* **2011**, *21*, 241.
(15) Poudeu, P. F. P.; D'Angelo, J.; Downey, A. D.; Short, J. L.; Hogan, T. P.; Kanatzidis, M. G. *Angew. Chem., Int. Ed.* **2006**, *45*, 3835.
(16) Androulakis, J.; Lin, C. H.; Kong, H. J.; Uher, C.; Wu, C. I.; Hogan, T.; Cook, B. A.; Caillat, T.; Paraskevopoulos, K. M.; Kanatzidis, M. G. *J. Am. Chem. Soc.* **2007**, *129*, 9780.
(17) Biswas, K.; He, J.; Zhang, Q.; Wang, G.; Uher, C.; Dravid, V. P.; Kanatzidis, M. G. *Nat. Chem.* **2011**, *3*, 160.
(18) Yang, S. H.; Zhu, T. J.; Sun, T.; He, J.; Zhang, S. N.; Zhao, X. B. *Nanotechnology* **2008**, *19*, 245707.
(19) Androulakis, J.; Todorov, I.; Chung, D.-Y.; Ballikaya, S.; Wang, G. Y.; Uher, C.; Kanatzidis, M. G. *Phys. Rev. B* **2010**, *82*, 115209.
(20) Biswas, K.; He, J. Q.; Blum, I. D.; Wu, C. I.; Hogan, T. P.; Seidman, D. N.; Dravid, V. P.; Kanatzidis, M. G. *Nature* **2012**, *489*, 414.
(21) Sootsman, J. R.; Chung, D. Y.; Kanatzidis, M. G. *Angew. Chem., Int. Ed.* **2009**, *48*, 861.
(22) Snyder, G. J.; Toberer, E. S. *Nat. Mater.* **2008**, *7*, 105.
(23) Brown, S. R.; Kauzlarich, S. M.; Gascoin, F.; Snyder, G. J. *Chem. Mater.* **2006**, *18*, 1873.
(24) (a) Wood, C. *Energy Con Version Manage.* **1984**, *24*, 331. (b) Yamashita, O.; Sadatomi, N. *J. Appl. Phys.* **2000**, *88*, 245. (c) Dismukes, J. P.; Ekstrom, L.; Steigmeier, E. F.; Kudman, I.; Beers, D. S. *J. Appl. Phys.* **1964**, *35*, 2899. (d) Atabaev, I. G.; Matchanov, N. A.; Bakhranov, E. N.; Saidov, M. S. *Inorg. Mater.* **2005**, *41*, 1033.
(25) (a) Catherine, A. C.; Brown, S. R.; Snyder, G. J.; Kauzlarich, S. M. *J. Electron. Mater.* **2010**, *39*, 1373. (b) Toberer, E. S.; Brown, S. R.; Ikeda, T.; Kauzlarich, S. M.; Snyder, G. J. *Appl. Phys. Lett.* **2008**, *93*, 062110. (c) Brown, S. R.; Toberer, E. S.; Ikeda, T.; Catherine, A. C.; Gascoin, F.; Kauzlarich, S. M.; Snyder, G. J. *Chem. Mater.* **2008**, *20*, 3412. (d) Rauscher, J. F.; Catherine, A. C.; Yi, T. H.; Beavers, C. M.; Klavins, P.; Toberer, E. S.; Snyder, G. J.; Kauzlarich, S. M. *Dalton. Trans.* **2010**, *39*, 1055. (e) Toberer, E. S.; Catherine, A. C.; Brown, S. R.; Ikeda, T.; May, A. F; Kauzlarich, S. M.; Snyder, G. J. *Adv. Funct. Mater.* **2008**, *18*, 2795. (f) Ribeiro, R. A.; Hadano, Y.; Suekuni, K.; Narazu, S.; Avila, M. A.; Takabatake, T. *J. Phys.: Condens. Matter* **2007**, *19*, 376211.
(26) (a) Zevalkink, A.; Toberer, E. S.; Zeier, W. G.; Flage-Larsen, E.; Snyder, G. J. *Energy Environ. Sci.* **2011**, *4*, 510. (b) Zeier, W. G.; Zevalkink, A.; Schechtel, E.; Tremel, W.; Snyder, G. J. *J. Mater. Chem.* **2012**, *22*, 9826.
(27) Zevalkink, A.; Zeier, W. G.; Pomrehn, G.; Schechtel, E.; Tremel, W.; Snyder, G. J. *Energy Environ. Sci.* **2012**, *5*, 9121.
(28) Gascoin, F.; Ottensmann, S.; Stark, D.; Haile, S. M.; Snyder, G. J. *Adv. Funct. Mater.* **2005**, *15*, 1860.
(29) Zhang, H.; Zhao, J.-T. *Dalton Trans.* **2010**, *39*, 1101.
(30) Zhang, H.; Fang, L.; Tang, M.-B.; Chen, H.-H.; Yang, X.-X.; Guo, X.-X.; Zhao, J.-T.; Grin, Y. *Intermetallics* **2010**, *18*, 193.
(31) Zhang, H.; Fang, L.; Tang, M.-B.; Man, Z. Y.; Chen, H. H.; Yang, X. X.; Baitinger, M.; Grin, Y.; Zhao, J.-T. *J. Chem. Phys.* **2010**, *133*, 194701.
(32) Guo, K.; Cao, Q.-G.; Feng, X.-J.; Tang, M.-B.; Chen, H.-H.; Guo, X.-X.; Chen, L.; Grin, Y.; Zhao, J.-T. *Eur. J. Inorg. Chem.* **2011**, 4043.
(33) Toberer, E. S.; May, A. F.; Melot, B. C.; Flage-Larsen, E.; Snyder, G. J. *Dalton Trans.* **2010**, *39*, 1046.
(34) May, A. F.; Toberer, E. S.; Snyder, G. J. *J. Appl. Phys.* **2009**, *106*, 013706.
(35) Toberer, E. S.; Zevalkink, A.; Crisosto, N.; Snyder, G. J. *Adv. Funct. Mater.* **2010**, *20*, 4375.
(36) Yi, T. H.; Cox, C. A.; Toberer, E. S.; Snyder, G. J.; Kauzlarich, S. M. *Chem. Mater.* **2010**, *22*, 935.
(37) Merlo, F.; Pani, M.; Fornasini, M. L. *J. Less-Common Met.* **1990**, *166*, 319.
(38) *Bruker APEX2*; Bruker AXS Inc.: Madison, WI, 2005.
(39) Sheldrick, G. M. *SHELXTL*; University of Göttingen: Göttingen, Germany, 2001.
(40) Parthé, E.; Gelato, L. M. *Acta Crystallogr.* **1984**, *A40*, 169.
(41) Gelato, L. M.; Parthé, E. *J. Appl. Crystallogr.* **1987**, *20*, 139.
(42) Madsen, G. K. H.; Blaha, P.; Schwarz, K.; Sjøstedt, E.; Nordström, L. *Phys. Rev. B* **2001**, *64*, 195134.

(43) Schwarz, K.; Blaha, P.; Madsen, G. K. H. *Comput. Phys. Commun.* **2002**, *147*, 71.
(44) Blaha, P.; Schwarz, K.; Madsen, G. K. H.; Kvasnicka, D.; Luitz, J. *WIEN2k, An Augmented Plane Wave + Local Orbitals Program for Calculating Crystal Properties*; Technische Universität: Vienna, Austria, 2001.
(45) Perdew, J. P.; Burke, S.; Ernzerhof, M. *Phys. Rev. Lett.* **1996**, *77*, 3865.
(46) Bockelmann, W.; Jacobs, H.; Schuster, H. U. *Z. Anorg. Allg. Chem.* **1974**, *410*, 233.
(47) Bojin, M. D.; Hoffmann, R. *Helv. Chim. Acta* **2003**, *86*, 1653.
(48) (a) Eisenmann, B.; Cordier, G.; Schaefer, H. *Z. Naturforsch.* **1974**, *29B*, 457. (b) Iandelli, A. *Rev. Chim. Miner.* **1987**, *24*, 28.
(49) Mori, T. In *Handbook on the Physics and Chemistry of Rare Earths*; Gschneidner, K. A., Jr.; Bunzli, J. C.; Pecharsky, V., Eds.; Elsevier: Amsterdam, 2008.
(50) Dilley, N. R.; Freeman, E. J.; Bauer, E. D.; Maple, M. B. *Phys. Rev. B.* **1998**, *58*, 6287.
(51) Qiu, P. F.; Yang, J.; Liu, R. H.; Shi, X.; Huang, X. Y.; Snyder, G. J.; Zhang, W.; Chen, L. D. *J. Appl. Phys.* **2011**, *109*, 063713.
(52) Ponou, S. *Eur. J. Inorg. Chem.* **2010**, 4139.
(53) Landrum, G. A.; Hoffmann, R. *Inorg. Chem.* **1998**, *37*, 5754.
(54) Yartys, V. A.; Olavesen, T.; Hauback, B. C.; Fjellvag, H.; Brinks, H. W. *J. Alloys Compd.* **2002**, *141*, 330.
(55) Malik, S. K.; Raj, P.; Sathyamoorthy, A.; Shashikala, K.; Kumar, N. H.; Menon, L. *Phys. Rev. B: Condens. Mater. Phys.* **2001**, *63*, 172418.
(56) Mott, N. F.; Jones, H. *The Theory of the Properties of Metals and Alloys*; Dover Publications: New York, 1958.
(57) Wang, J.; Xia, S.-Q.; Tao, X.-T. *Chem.—Asian J.* **2013**, *8*, 25.
(58) Goldsmid, H. J.; Sharp, J. W. *J. Electron. Mater.* **1999**, *28*, 869.
(59) Liu, Y.; Zhao, L.-D.; Liu, Y.-C.; Lan, J.-L.; Xu, W.; Li, F.; Zhang, B.-P.; Berardan, D.; Dragoe, N.; Lin, Y.-H.; Nan, C.-W.; Li, J.-F.; Zhu, H.-M. *J. Am. Chem. Soc.* **2011**, *133*, 20112.
(60) Snyder, G. J.; Christensen, M.; Nishibori, E.; Caillat, T.; Iversen, B. B. *Nat. Mater.* **2004**, *3*, 458.
(61) Chitroub, M.; Besse, F.; Scherrer, H. *J. Alloys Compd.* **2008**, *460*, 90.
(62) Pei, Y. Z.; Wang, H.; Snyder, G. J. *Adv. Mater.* **2012**, *24*, 6125.
(63) Uvarov, C. A.; Ortega-Alvarez, F.; Kauzlarich, S. M. *Inorg. Chem.* **2012**, *51*, 7617.